Nanoscale phase-slip domain walls in the charge density wave state of the Weyl semimetal candidate math xmlns="http://www.w3.org/1998/Math/MathML">msub>mi >NbTe/mi>mn>4/mn>/msub>/math>

J. A. Galvis, A. Fang, D. Jiménez-Guerrero, J. Rojas-Castillo, J. Casas, O. Herrera, A. C. Garcia-Castro, E. Bousquet, I. R. Fisher, A. Kapitulnik, and P. Giraldo-Gallo

Phys. Rev. B **107**, 045120 — Published 17 January 2023

DOI: 10.1103/PhysRevB.107.045120

Nanoscale phase-slip domain-walls in the charge density wave state of the Weyl semimetal candidate $NbTe_4$

J. A. Galvis,[1] A. Fang,[2,3] D. Jiménez-Guerrero,[4] J. Rojas-Castillo,[4] J. Casas,[1] O. Herrera,[1] A. C. Garcia-Castro,[5] E. Bousquet,[6] I. R. Fisher,[2,3] A. Kapitulnik,[2,3] and P. Giraldo-Gallo†[4]

[1] *Faculty of Engineering and Basic Sciences, Universidad Central, Bogotá, Colombia*
[2] *Department of Applied Physics and Geballe Laboratory for Advanced Materials, Stanford University, Stanford, California 94305, USA*
[3] *Stanford Institute for Materials and Energy Sciences, SLAC National Accelerator Laboratory, 2575 Sand Hill Road, Menlo Park, California 94025, USA*
[4] *Department of Physics, Universidad de Los Andes, Bogotá 111711, Colombia*
[5] *School of Physics, Universidad Industrial de Santander, Carrera 27 Calle 09, 680002, Bucaramanga, Colombia*
[6] *Physique Théorique des Matériaux, QMAT, CESAM, Université de Liège, B-4000 Sart-Tilman, Belgium*

(Dated: January 3, 2023)

The transition-metal tetrachalcogenides are a model system to explore the conjunction of correlated electronic states such as charge density waves (CDW), with topological phases of matter. Understanding the connection between these phases requires a thorough understanding of the individual states, which for the case of the CDW in this system, is still missing. In this paper we combine phonon-structure calculations and scanning tunneling microscopy measurements of $NbTe_4$ in order to provide a full characterization of the CDW state. We find that, at short range, the superstructure formed by the CDW is fully commensurate with the lattice parameters. Moreover, our data reveals the presence of phase-slip domain-walls separating regions of commensurate-CDW in the nanoscale, indicating that the CDW in this compound is discommensurate at long-range. Our results solve a long-standing discussion about the nature of the CDW in these materials, and provide a strong basis for the study of the interplay between this state and other novel quantum electronic states.

Keywords: Transition metal chalcogenides, $NbTe_4$, charge density wave, Weyl-semimetals, extended-domain-walls, CDW phase-slip.

1. INTRODUCTION

Transition-metal chalcogenides are a model family to study a large variety of quantum phenomena including charge density wave (CDW) formation, superconductivity, topological states and magnetism [1–3]. Among this family, the quasi-1-dimensional transition-metal tetrachalcogenides, with their representative members: $NbTe_4$ and $TaTe_4$, have recently gained a renewed interest due to the possibility of hosting axionic states connecting different Weyl-points in the Fermi-surface through the formation of a CDW [4–6]. Therefore, these compounds provide an ideal opportunity to study the connection between topological states of matter and correlated electronic states such as CDWs [7, 8]. In addition, recent high-pressure experiments have reported the presence of superconductivity in both, $NbTe_4$ [9] and $TaTe_4$ [10], making them strong candidates for a new class of topological superconductors. All of these novel phenomena motivate a thorough characterization of the different physical properties of these materials, in particular, of the details and origin of the CDW at low-temperatures, where the possible topological properties are more likely to be observed.

The crystal structure of $NbTe_4$ originates from subtle deformations of its high-temperature tetragonal space group *P4/mcc*, shown in figure 1(a,b), with reported unit cell parameters a, b=6.499 Å and c=6.837 Å at room-temperature, and confirmed by our x-ray data (fig. 1c) [13]. In this structure, Nb-atoms are at the center of two square antiprisms of Te-atoms, each rotated with respect to the other (fig. 1a). These units form linear chains in the c-direction (fig. 1b), which are bonded to other chains by van der Waals interactions. As a consequence, single crystals of this compound grow as long-needles parallel to the c-axis, which evidences the quasi-one-dimensional character of its crystal structure.

X-ray and electron diffraction studies in $NbTe_4$ have revealed distortions from the *P4/mcc* structure, and have associated those to several possible CDW distortions [7, 14, 15]. A variety of satellite peaks and streaks in the diffraction patterns develop at different temperatures and the appearance of such features roughly coincide with features observed in electrical resistivity measurements (see vertical-dashed-lines in fig. 1(d,e) for some of such features) [12]. At room-temperature, satellite peaks at $\boldsymbol{q_1} = (\frac{1}{2}a^*, \frac{1}{2}a^*, (\frac{2}{3}+\delta)\,c^*)$, $\boldsymbol{q_2} = (0, 0, (\frac{2}{3}-2\delta)\,c^*)$, $\boldsymbol{q_3} = (0, 0, (\frac{2}{3}+4\delta)\,c^*)$, where a^* and c^* are the inverse

† Corresponding author: pl.giraldo@uniandes.edu.co

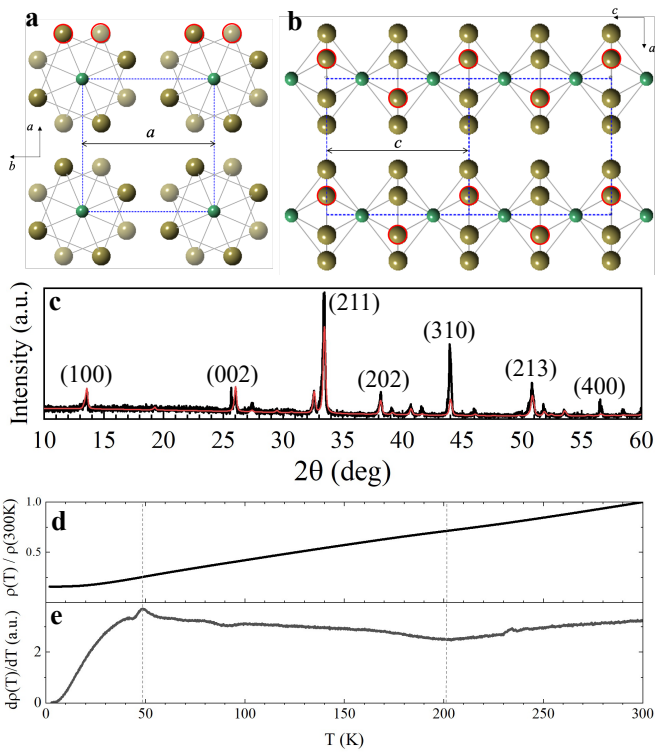

FIG. 1. (Color online) **(a)** Crystal structure of $NbTe_4$, with space group **P4/mcc** (SG. 124) projected along the **(a)** [001] and **(b)** [010] directions. The Te-atoms with red borders in (a) and (b) are atoms forming a cleaved {010} surface. **(c)** Powder X-ray diffraction measurements of ground single crystals (black-line), with diffraction peaks consistent with the **P4/mcc** space group (refinement in red). **(d)** Temperature dependence of the resistivity, normalized by the room-temperature value. The residual resistivity ratio (RRR) is 6.3, similar to previously reported studies [9, 11, 12]. **(e)** Derivative of the normalized resistivity curve in (d). Vertical-dashed-lines indicate changes in the temperature dependence of the resistivity, previously associated to CDW-transitions.

of a and c, respectively, and $\delta = 0.022$ (following the notation of *Eaglesham et al.*) are observed by selected-area diffraction patterns as reported by several authors [15–17]. Below approximately 210 K to 180 K (varies for different authors and on cooling/warming history), diffuse streaks at different positions of the reciprocal space are progressively developed, and are even reported to evolve into regularly spaced spots as temperature is decreased [15]. Below about 50 K, the different satellite diffraction peaks become commensurate with the *P4/mcc* lattice parameters (meaning, $\delta = 0$), and the $\boldsymbol{q_2}$ and $\boldsymbol{q_3}$ peaks merge into one ($\boldsymbol{q_2} = (0, 0, \frac{2}{3}c^*)$). This has been interpreted as a lock-in (incommensurate-to-commensurate) transition of the CDW distortion [16].

Although the characterization of the lattice distortion and reciprocal space mapping of $NbTe_4$ by diffraction experiments has been extensive, direct observation of the CDW modulation by real-space imaging techniques is scarce. Previous scanning tunnelling microscopy (STM) data attempted to characterize the charge modulation at room-temperature, however, with a limited resolution [18]. To our knowledge, there are no previous reports of the observation of the low-temperature CDW modulation of $NbTe_4$ by STM experiments. Recent experiment in the other family member of the tetrachalcogenides, $TaTe_4$, reported on the observation of a new type of charge modulation, distinct from the ones reported by diffraction experiments, presumably coming from surface effects in this compound [6]. All of these observations motivate a thorough characterization of the low-temperature CDW states in $NbTe_4$ by direct imaging and spectroscopic techniques.

In this article we report on a combination of low-temperature STM measurements and phonon dispersion calculations of the quasi-1D transition-metal tetrachalcogenide $NbTe_4$. Our measurements of the low-temperature charge distribution in the {010} plane directly reveal, for the first time, the superstructure created by the CDW in this material, which agrees with our theory predictions. Furthermore, we present evidence for the presence of a discommensurate-CDW (i.e., commensurate regions separated by phase-slip domain-walls) at low-temperature, with wavevector and phase-slip conditions consistent with the features reported by previous diffraction experiments *at room-temperature*, although our measurements are performed at 1.7 K. This observation suggests that the CDW in this compound is discommensurate for all temperatures below room-temperature, therefore inviting to revisit the characteristics and conditions of the presumable lock-in transition and other intermediate-temperature transitions reported for this material. Our results provide strong evidence to solve a long-standing discussion around the characteristics of the CDW in this material, and provides a strong basis for the study of the interplay between this state and other novel quantum electronic states, such as the recently predicted Weyl-points.

2. MATERIALS AND METHODS

2.1. Computational Approach

The density functional theory (DFT) [19, 20] calculations were performed with the ABINIT package (v8.11.8) [21, 22]. The norm-conserving pseudopotentials from the PseudoDojo project (v0.4) [23] were used with the generalized gradient approximation PBEsol exchange correlation functional [24] and a Fermi-Dirac electronic smearing of 0.001 Hartree (Ha). The phonon calculations were performed using the density functional perturbation theory (DFPT) [25] and a good convergence (about 1 cm^{-1} on the frequencies) was obtained with a k-points mesh of

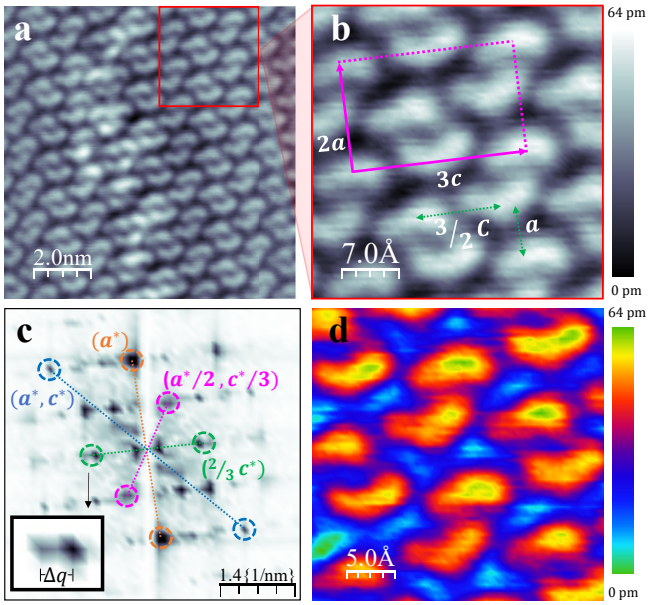

FIG. 2. **(a)** Scanning tunneling topography image of a cleaved $NbTe_4$ single crystal. The CDW superstructure formed at the Te-terminated surface is observed. The area enclosed by the red square is magnified in **(b)** in which the unit cell of the superstructure (pink square), with size $2a\times3c$, can be clearly identified. **(c)** Fourier transform of the image shown in (a). Different peaks have been highlighted by different-color circles. The peaks highlighted by the pink-circles correspond to the CDW superstructure unit cell. The peaks highlighted by the green-circles correspond to the distance between adjacent "cashews" (Te-trimers) with opposite curvature, along the c-direction, this is, with central $q = (0, \frac{2}{3}c^*)$. Theses peaks are split, as better seen in the inset. **(d)** Close-up look to a STM image, presented using a color scale that highlights the asymmetry in the charge distribution of the cashews or Te trimers. The maximum of the scale (yellow-colors) is shifted toward the right-side for all cashews, independent of their orientation (facing up or down).

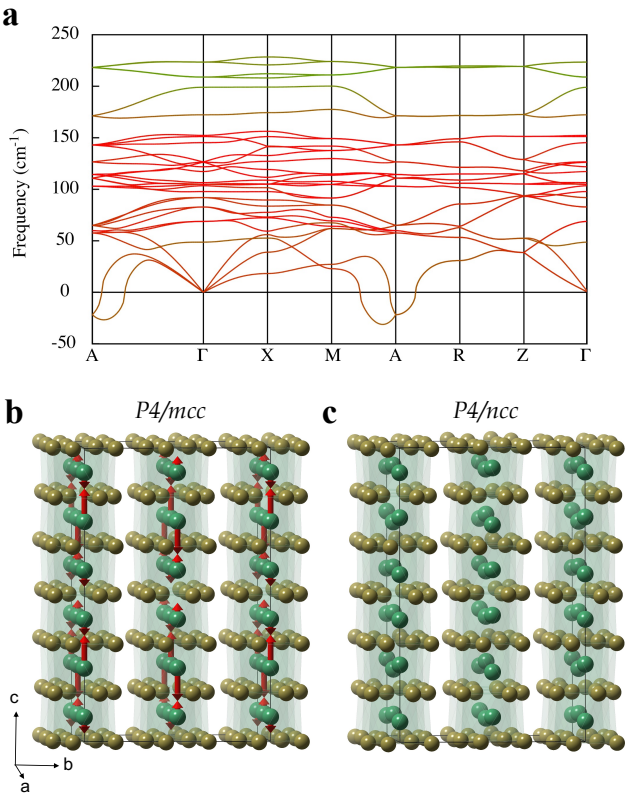

FIG. 3. (Color online) **(a)** Calculated phonon dispersion curves along various paths between high-symmetry points in the *P4/mcc* Brillouin zone of $NbTe_4$. The unstable modes with imaginary frequencies are presented by negative values on the plot. The dispersion line color has been assigned to each point according to the contribution of each kind of atom to the associated eigenvector (red for Nb and blue for Te). **(b)** Schematic picture of the eigendisplacements of the V_4 unstable phonon at the q=($^1/_2$,$^1/_2$,$^1/_3$) vector, the atom displacements are shown as red-arrows in the high-symmetry *P4/mcc* phase. **(c)** Fully relaxed modulated *P4/ncc* structure is presented.

$8 \times 8 \times 8$ in the reciprocal space and a cutoff energy for the plane wave expansion of 35 Ha. The phonon dispersions were interpolated with a grid of $4 \times 4 \times 4$ q-points in the reciprocal space. The symmetry adapted mode contributions to the phase-transition was analyzed using the AMPLIMODE software [26].

2.2. Experimental Methods

Single crystals of $NbTe_4$ were grown using a self-flux technique [27]. A mixture of 1 mol% of elemental Nb and 99 mol% of elemental Te were put in alumina crucibles and sealed in evacuated quartz tubes. The mix was heated to 700°C, held at this temperature for 12 hours and then slowly cooled to 500°C at a rate of 2°C/hour. The remaining melt was decanted and separated from the $NbTe_4$ crystals using a centrifuge. Silver-colored long rectangular prism shaped crystals were obtained, with sizes up to $0.1 \times 0.1 \times 1$ cm^3.

Powder X-ray diffraction measurements were taken from a collection of ground single crystals, in Eulerian-Cradle geometry, using a Panalytical X-Pert system. Resistivity measurements as a function of temperature (Fig. 1d,e) were taken in cleaved crystals using a four-probe configuration, with electrical current running along the c-direction. Electrical contact was made using sputtered gold pads. A ^{4}He VTI-cryostat was used to vary temperature from room-temperature down to 2 K.

STM was performed with a hybrid UNISOKU-USM1300 system constructed with a homemade ultrahigh-vacuum sample preparation and manipulation system. The samples were cleaved at room-temperature at pressures lower

than 10^{-10} torr and immediately transferred to the low temperature STM. Crystals cleave exposing the {010} surface, this is, the a-c plane. All topographies were performed at 1.7 K, with tunneling parameters of V_{bias} = 100 mV and I=100 pA.

3. RESULTS AND DISCUSSION

3.1. Short-range STM measurements

Figure 2 shows STM measurements taken at the {010} surface of a $NbTe_4$ crystal. The cleaved-surface that is observed in the image is formed by Te-atoms in the a-c plane, as the bonding between Te-atoms is weaker than between Nb and Te [13], a common feature in all low-dimensional transition-metal chalcogenides. The Te-atoms expected to be observed in the surface are highlighted in red-circles in Fig. 1b, forming zig-zag chains that run along the c-direction. The large-scale topographic image (figure 2a) reveals a periodic modulation of the electronic density, formed by rows of cashew-shaped units with alternating up-down curvatures, and with adjacent rows shifted 1/3 of a row period. This modulation forms a superstructure with unit cell as highlighted by the pink-rectangle in the close-up look to the topographic image, shown in fig. 2b. The spatial periodicity can be accurately determined through the fast Fourier transform (FFT) in Fig. 2c, resulting in a $2a \times 3c$ periodicity (FFT peaks labeled as $(a^*/2, c^*/3)$). The size of this superstructure matches the commensurate-CDW superstructure reported by several diffraction experiments at low-temperatures (<50 K) [7, 16, 17]. We will later discuss other important features of the FFT of the topographic image.

3.2. Phonon-dispersion calculations

In order to explain the superstructure shown by the topography images and the origin of the CDW modulation in $NbTe_4$, we have computed the vibrational landscape of the high-symmetry structure $P4/mcc$ (space group (SG) 124). Fig. 3a shows the calculated phonon-dispersion curves of the $P4/mcc$ high-symmetry structure. An instability appears at the A ($1/2$,$1/2$,$1/2$) high-symmetry point of the Brillouin zone (with the irreducible representation – irrep – A_2), which disperses quickly when going away from the A point. However, the strongest unstable phonon frequency is located in a point between the A and M point, in a region close to q=($1/2$,$1/2$,$1/3$) (irrep V_4). To resolve the lowest energy structure, we condensed the A_2 and V_4 unstable mode eigenvectors into two different structures, with $2a\times2a\times2c$ and $2a\times2a\times3c$ supercells with respect to the high-symmetry unit cell, respectively. We find that the phase formed by the V_4 mode (which leads to the $P4/ncc$ - SG 130) has a lower energy than the phase formed by the A_2 mode ($I4$ - SG 79). This result is in good agreement with the observed $2a\times3c$ superstructure seen at low-temperatures in our STM data. Interestingly, our calculations show that the V_4-mode is strongly driven by the Nb-sites with a small deviation, from the high-symmetry position, of the Te-

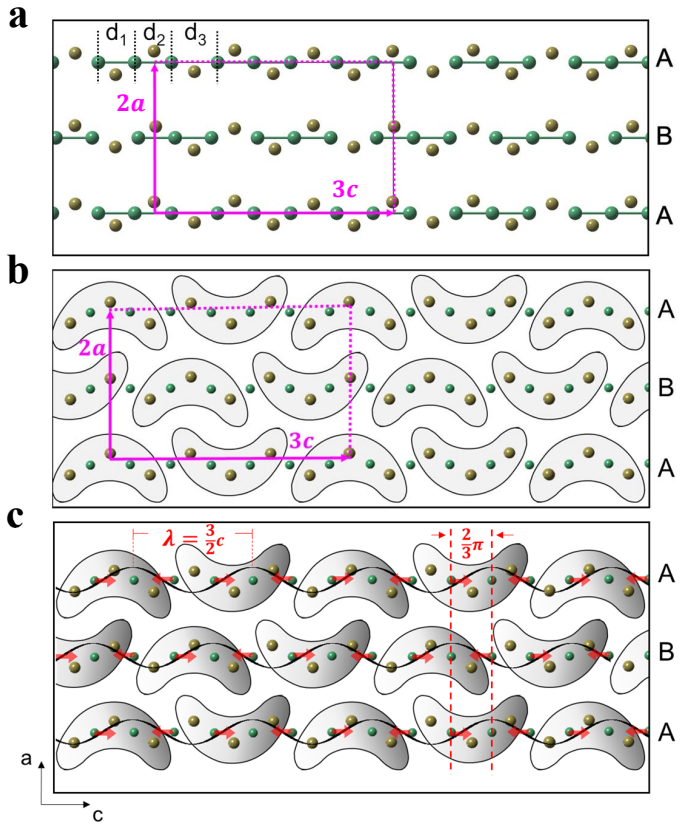

FIG. 4. (Color online) All figures show the Te-atoms (dark-yellow balls) of three chains in a {010} cleaved-surface, as well as the closest Nb-atoms (green balls) underneath this surface. **(a)** Spatial configuration of the Nb-trimers in the final modulated structure as calculated by our DFT model. Three nonequivalent distances between the Nb-atoms are found in the model, with two short (d_1 and d_2) and one long (d_3), therefore forming Nb-trimers as represented by the green solid-lines. The unit cell of the Nb-trimers superstructure is indicated by the pink rectangle. A-B-A refers to the stacking of the chains. **(b)** Representation of the Te-trimer formation, which leads to the cashew-shapes observed in the topographic images. The unit cell of the Te-trimers superstructure is indicated by the pink rectangle, matching the unit cell of the Nb-trimers superstructure. **(c)** Red-arrows in this figure indicate a simplified representation of the Nb-atoms displacements, which lead to the CDW modulation in this compound. The charge density is maximum around the center of each Nb-trimer, which coincides with the right-side of the cashews, generating their asymmetric charge density (gradient color-fill). The charge density amplitude variation is depicted by the black-waves. The wavelength of the CDW is $\lambda = 3c/2$, and the phase-shift between adjacent chains is $\pm 2\pi/3$.

sites. Fig. 3b shows the undistorted $P4/mcc$ phase in which the most significant atomic displacements of the V_4-mode are depicted by red-arrows. Once these distortions are condensed and the structure fully relaxed, the obtained structural modulation can be observed in Fig. 3c. In such a phase, the modulation induces a trimerization of the Nb-sites in the 1D-chains. The three Nb−Nb distances, d_{Nb-Nb}, are 3.137 Å, 3.168 Å and 3.971 Å, hence, two short and one long. This result is in line with suggestions from previous works [14, 28]. Fig. 4a shows the spatial configuration of the Nb-trimers that lie just underneath a cleaved-surface, in the final modulated structure, as calculated by our DFT model. This figure highlights the A-B-A stacking of the trimers in adjacent chains, with the B-chain trimers shifted by one Nb-atom to the right (or two Nb-atoms to the left), or equivalently, $c/2$ to the right (or c to the left), with respect to the A-chain trimers. This specific A-B-A stacking of the chains is responsible for the $2a$ periodicity of the superstructure along the direction perpendicular to the chains.

3.3. CDW-structure

The trimerization of Nb-atoms, predicted by our DFT calculations, has important consequences for the charge distribution in the cleaved-surface of the $NbTe_4$ crystals. As mentioned previously, this surface is formed by Te-atoms. The schematic configurations shown in fig. 4a,b,c show these surface Te-atoms in a {010} cleaved-surface, together with the Nb-atoms just underneath this surface. The cashew-shapes observed in our topographic images can be naturally explained by the trimerization of the Te-atoms in the surface, which are arranged in zig-zag along the chains, as represented in fig. 4b (see fig. A1, in Appendix A, for an image that reveals the internal structure of a cashew). The formation of Te-trimers (or cashews) is a consequence of the trimerization of the Nb-atoms underneath. This trimerization also naturally explains the alternating up-down curvature of successive cashews within a chain. The cashew configuration along each chain, with period $3c$, is shifted by c in both -up and down- adjacent chains (to the left if taken with respect to the middle-B-chain in fig. 4b, or equivalently, $2c$ to the right), and in the same direction for both adjacent chains. This specific A-B-A stacking of the chains is fully equivalent to the one found in our DFT calculations, and reproduces the unit cell of the superstructure, with period $2a \times 3c$, observed by our topographic images.

Noteworthy, the charge distribution within a single cashew-like structure is asymmetric, as is better appreciated in fig. 2d. The position where the maximum charge distribution occurs, as observed in the topography image, is shifted toward the right side on each cashew. This asymmetry is an indication that the CDW distortion indeed originates in the Nb-atoms, instead of the Te-atoms, in full agreement with our DFT calculations. Fig. 4c shows a simplified schematic representation of the Nb-atoms displacements that give rise to such an asymmetric Te-surface charge distribution. In this picture, the central Nb-atom of each Nb-trimer, where charge density is expected to be higher, is located toward the right-end of the Te-trimer, which could explain the accumulation of charge toward the right-side of the cashews in the observed Te-surface. Within this picture, the CDW is represented by the waves depicted in Fig. 4c, with a maximum amplitude right at (or very close to) the center of the Nb-trimer (which coincides with the right side of each Te-trimer or cashew), and a minimum amplitude in the space between two Nb-trimers. The wavelength of this CDW is $\lambda = 3c/2$, and it therefore implies a CDW-wavevector within each chain of $q_{CDW} = (0, 0, 2c^*/3)$. Waves in both -up and down - adjacent chains of each chain are shifted by $2\pi/3$ either both to the left or both to the right, generating the observed A-B-A stacking of the superstructure. As a consequence of the CDW-wavector and the phase-shifts in adjacent chains, the observed superstructure in the Te-atoms-surface has a periodicity of $2a \times 3c$, as revealed by our topographic images, and predicted by our DFT calculations. Therefore, the phonon-mode responsible for such a commensurate distortion is the V_4-mode.

Tunneling conductance curves reveal the presence of a gap of $2\Delta \approx 24$ meV (see Fig. A4 in Appendix C). However, this value is an order of magnitude lower than the expected gap originated in a CDW distortion with T_C above room temperature, as reported for this material [7]. This suggests the presence of an electronic instability of different origin (see Appendix C).

3.4. Wide-area STM measurements: phase-slip domain walls

We will now discuss the intricacies of the FFT, which reveal the presence of discommesurations of the CDW in $NbTe_4$. The FFT (fig. 2c) of the topographic image of fig. 2a reveals other intense peaks, in addition to the $(a^*/2, c^*/3)$ peaks of the superstructure unit cell. Interestingly, the peak around $(0, 2c^*/3)$ (highlighted in the green-circle) is split in two, as can be better observed in the inset to this figure. Although the presence of split peaks as well as the presence of other satellite peaks in diffraction experiments have been interpreted as signatures of incommensurate CDWs [7, 15, 29], we argue that all satellite peaks observed by diffraction experiments in all ranges of temperatures are a consequence of discommensurations of a unique commensurate CDW-phase, this is, regions of commensurate CDW separated by domain-walls. Figure 5a shows a wide-area topographic image of a cleaved $NbTe_4$ surface. Long columnar features along the a-direction, and running from top-to-

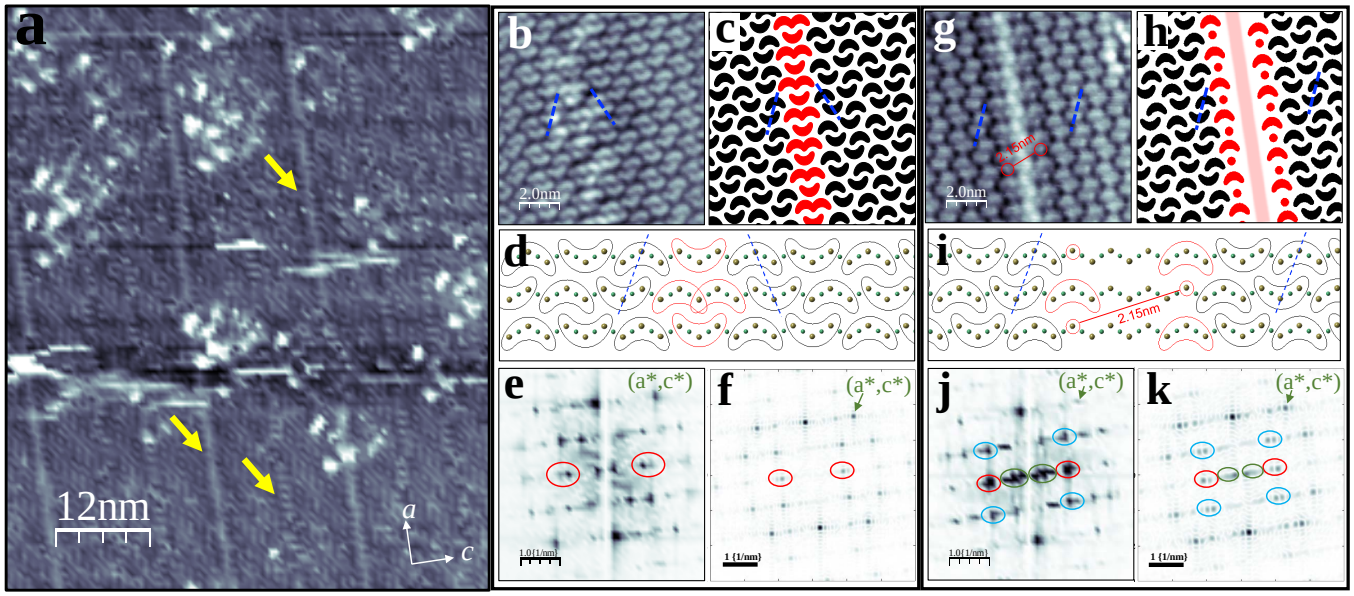

FIG. 5. (Color online) **(a)** Wide-area STM topographic image of a cleaved $NbTe_4$ single-crystal showing different domain-walls (some are highlighted by the yellow-arrows) which run over long distances along the a-direction. **(b)** and **(g)** show topographic images taken at a reduced area (therefore with an improved resolution), in which two different types of domain-walls can be recognized (see fig. A3 for five other types of domain walls). **(c)** and **(h)** show schematic representations of the cashews configuration across the domain-walls in (b) and (g), respectively. The cashews forming the domain-walls are represented in red. The blue-dashed-lines represent the sign of the phase-shift of the CDWs of two adjacent chains: a change in inclination represents a change of phase sign. The schematic representations in (c) and (h) capture the change of sign of this phase-difference at the left-side and right-side of the domain-walls. **(d)** and **(i)** show the atomic configuration of the Te-atoms at the surface (and the Nb-atoms underneath) which lead to the domain-walls of (b,c) and (g,h), respectively. **(e,f,j,k)** show the FFT of the images in (b,c,g,h), respectively. Red-ovals in all FFTs highlight the $(0, 2c^*/3)$ peaks, which splitting is reproduced in the real-images FFTs and the schematic representation FFTs. Blue-ovals in the FFTs of (j,k) highlight the $(a^*/2, 2c^*/3)$ peaks, which are split for the second type of domain-wall (g-k), but not for the first type (b-f). Green-ovals in the FFTs of (j,k) highlight peaks along the horizontal-axis and close to the origin, which are present for the second type of domain-wall, but not for the first type.

down all through the image, can be observed (yellow-arrows highlight three of those columns). Careful and closer inspection to different areas containing such columnar features reveal different patterns. Two examples of the type of features that can be found are shown in Figs. 5b (same as in fig. 2a) and fig. 5g. The FFT of these images (figs. 5e and 5j, respectively) show marked differences. For instance, whereas the $(0, 2c^*/3)$ peaks of the first type of domain-wall are split, the $(a^*/2, 2c^*/3)$ peaks are not. In contrast, both of those set of peaks are split for the second type of domain-wall and, furthermore, additional peaks along the horizontal-axis close to the origin (green-ovals) appear in its FFT. Fig. 5c shows a cartoon model of the distortion of the cashews pattern for the first type of domain wall (highlighted in red). This type of domain-wall can be generated by the situation depicted in fig. 5d in which, within a chain, two nearest-neighbors Nb-trimers share one atom (or site). This implies a CDW phase-slip of $2\pi/3$ to the left within the chain, which results in the partial-merge of two cashews for the Te-trimers at the surface and therefore, the flip on the orientation of one of the cashews. The Nb (and Te) trimers in adjacent chains remain intact creating a domain-wall with alternating double-simple cashews. One way to validate this picture is observing the flip in CDW phase-difference between successive chains on the left and right of the domain-wall: with respect to the top-chain in fig. 5d the CDW-phase of the middle row is shifted $2\pi/3$ to the left, on the left of the domain-wall, but $2\pi/3$ to the right, on the right of the domain-wall. This is represented by the flip in orientation of the dashed-blue-lines in figs. 5(b,c,d). The FFT of the cartoon model in fig. 5c is shown in fig. 5f, and it reproduces the main features observed in the FFT of the corresponding real topographic image. The second example of domain-wall (in fig. 5g) is represented by the cartoon model in fig. 5h. This pattern can be obtained by the situation shown in fig. 5i in which five Nb-atoms within a chain are not clearly bound to trimers, deriving in a CDW phase-slip of $4\pi/3$ to the right (or $2\pi/3$ to the left) within each chain. This phase-slip happens for every chain (row) in the structure, which implies an equivalent CDW interchain phase-shift at the right and left of the domain-wall (situation highlighted by the dashed-blue-lines in figs. 5(g,h,i)), in contrast

with the first example of domain-wall. The FFT of the cartoon model is shown in fig. 5k, and also reproduces the main features of the FFT of the corresponding real topographic image.

Other types of domain-walls, different from the two examples discussed previously, can be found within our topographic images (see appendix fig. A3). In principle, a domain-wall can be created by any possible combination of phase-slips for different chains. Nevertheless, only intrachain CDW phase-slips of $\pm 2\pi/3$ (or equivalently, $\pm n * c/2$ displacements of cashews, where n is an integer) are allowed by the symmetry of the crystal structure and the CDW-wavelength, which limits the possibilities for domain-wall configurations. This constrain in the phase-slip can be the reason for the finite set of satellite peaks found in diffraction experiments. In addition, the splitting of the $(0, 2c^*/3)$ peaks seen in this work is comparable to the one reported by diffraction experiments by several authors [7, 15–17]. This highly suggests that, what had been interpreted before as signatures of the presence of incommesurate CDWs in $NbTe_4$ (as, for example, in refs. [7, 9, 11, 15, 16, 18, 29]) are, on the other hand, signatures of discommensurations due to phase-slip domain-walls (as previously suggested in refs. [16, 17, 30]), which separate regions of commensurate-CDW with wavevector $q_{CDW} = (0, 0, 2c^*/3)$ within a chain, phase-difference of $\pm 2\pi/3$ with adjacent chains, and ABA stacking.

An important characteristic of the domain-walls is that they run over large distances along the same line in the a-direction, with no (or minor) disruptions, and are not necessarily periodic along the c-direction (the $(0, 2c^*/3)$ peak splitting does not come from a periodic arrangement of domain walls, but instead, from the repeated phase-slip along multiple chains involved in a single domain wall, as shown in appendix B and appendix fig. A2). The highly coherent domain-walls along the a-direction may be a consequence of the interchain coupling strength, which for $NbTe_4$ is much more significant than for other low-dimensional transition-metal chalcogenides. For instance, the interchain Te-Te distance in the tetrachalcogenides is shorter than the intrachain Te-Te distance, which has been predicted to result in the formation of interchain Te-Te dimers that can hybridize with the transition-metal atoms, leading to a large metallic conduction in the direction perpendicular to the chains [28, 31]. In fact, the resistivity anisotropy of $NbTe_4$ has been reported to be very close to 1 [12], unexpected for such an anisotropic quasi-1D crystalline structure. The results presented by our study inspire relevant question that can help understanding these electronic properties. For example, the large tunnel conductance values observed in some of the domain-walls, which could be an indication of a largest charge density, invites to study the domain-walls contribution to the electronic conductance in the a-direction. On the other hand, similarly long and coherent columnar domain-walls have been observed in other low-dimensional systems (for example, graphene nanostructures [32]), in which topological defects due to atomic vacancies in the crystalline structure form extended dislocations. A similar mechanism could also be the origin of the observed CDW domain-walls in $NbTe_4$, possibly originated by Te-vacancies. Another relevant question is the influence of random quenched disorder on the domain-wall density, coherence length, and even CDW fundamental properties, as observed for other prototypical CDW systems [33].

3.5. Wider implications

It is important to emphasize that our STM measurements have been performed at low-temperature, and not at room-temperature. The presence of split peaks in diffraction experiments have been reported at room-temperature, with the appearance of other streaks and peaks as temperature is lowered. The equivalent characteristics of the FFTs of our topographic images and the ones reported by diffraction experiments suggest that the CDW in $NbTe_4$ is discommensurate and with an unchanged CDW-wavevector from room-temperature down to 1.7 K. Nevertheless, resistivity measurements as a function of temperature (see fig. 1d,e) reveal marked changes of slope at certain temperatures (both in our data and data taken by other authors), which have been historically interpreted as CDW phase-transitions. Interestingly, a temperature of $\sim$50 K, at which a marked feature in the derivative of the ρ vs T curve appears (see fig. 1e), seems to coincide with the temperature below which the peak splitting and presence of diffuse streaks disappear in electron diffraction experiments, which has been interpreted as a lock-in (incommensurate-to-commensurate) transition of the CDW. As argued, the features observed in diffraction experiments could be explained by discommensurations, rather than incommensurations of the CDW, inviting to consider the configuration and dynamics of the phase-slip domain-walls as possible candidates driving the presumed phase-transitions suggested by the features in resistivity curves and diffraction experiments (as observed in other CDW systems [34]). Evidence supporting this scenario can be found in a previous electron diffraction study in $NbTe_4$ in which indications of discommensuration arrays with a varying density as a function of temperature were reported [30]. The disappearance of peak splitting in diffraction experiments below 50 K could be related to a significant reduction of domain-wall density. Given the much wider sample areas involved in diffraction experiments, compared to STM, a low density of domain walls might not be enough for resolving the peak splitting in diffraction given their low statistical weight. However, as STM typically measures much smaller areas, the presence of a couple of domain walls can enhance the signal of the peak splitting

given their larger statistical weight in the smaller area.

Finally, it is pertinent to highlight that our topographic data can be fully reproduced by the condensed V_4 phonon-instability predicted by our DFT calculations. This indicates that an electron-phonon coupling mechanism is largely responsible for the commensurate-CDW formation in this compound, in contrast to the Fermi-surface nesting or Peierls mechanism commonly expected in low-dimensional compounds [35]. This observation is in line with previous works suggesting the electron-phonon mechanism as the dominant driving force for CDW formation in most real materials, even in the 1D limit [28, 36]. Since the transition-metal tetrachalcogenides have been predicted to host Weyl-nodes in their electronic structure, our results motivate further theoretical and experimental studies aimed at understanding the influence of electron-phonon coupling on the determination of complex Fermi-surface topologies and its connection with novel topological quasiparticles in materials [37–39].

4. SUMMARY AND CONCLUSIONS

Through the combination of low-temperature STM measurements and phonon dispersion calculations we have determined the characteristics and origin of the CDW in the quasi-1D transition-metal tetrachalcogenide $NbTe_4$. In the nanoscale, the CDW is commensurate with the lattice parameters, with a CDW-wavevector within each chain of $q_{CDW} = (0, 0, 2c^*/3)$. Waves in both up- and down- adjacent chains of each chain are shifted by $2\pi/3$ either both to the left or both to the right, generating an A-B-A chain stacking. As a consequence of the CDW-wavector and the phase-shifts in adjacent chains, the observed superstructure in the Te-atoms-surfaces has a periodicity of $2a \times 3c$. Such CDW originates in a V_4 unstable phonon-mode and an electron-phonon coupling mechanism, in contrast to the Peierls-like mechanism expected to dominate in low-dimensional systems.

In the long range, the CDW is discommensurate, i.e., commensurate CDW regions separated by phase-slip domain-walls, with wavevector and phase-slip conditions consistent with the features reported by previous diffraction experiments *at room-temperature*, although our measurements are performed at 1.7 K. This observation suggests that the CDW in this compound is discommensurate for all temperatures below room-temperature, therefore inviting to revisit the characteristics and conditions of the presumable lock-in transition and other intermediate-temperature transitions reported for this material. Our results provide strong evidence to solve a long-standing discussion around the characteristics of the CDW in this material, and provides a strong basis for the study of the interplay between this state and other novel quantum electronic states, such as the recently predicted Weyl-states.

ACKNOWLEDGEMENTS

The authors thank C. A. Mera, L. Quiroga, F. Rodriguez, H. Suderow, I. Guillamon and E. Herrera for enlightening discussions. J.A.G., D.J-G., J.R-C., J.C., O.H. and P.G-G. thank the support of the Ministerio de Ciencia, Tecnología e Innovación de Colombia (Grants No. 120480863414 and No. 122585271058). P.G-G. and I.R.F. thank the support of the APS International Travel Grant Award Program which enabled P.G-G. to visit Stanford University. P.G-G. thanks the support of the L'Oréal-UNESCO For Women in Science International Rising Talents Programme, the School of Sciences and the Vice Presidency of Research Creation at Universidad de Los Andes. J.A.G., J.C. and O.H. thank the support of Clúster de Investigación en Ciencias y Tecnologías Convergentes NBIC, Universidad Central. I.R.F., A.F. and A.K. were supported by the Department of Energy, Office of Basic Energy Sciences, under contract DE-AC02-76SF00515.
This work used the DECI PRACE project OFFSPRING and the CECI facilities funded by F.R.S-FNRS (Grant No. 2.5020.1) and Tier-1 supercomputer of the Fédération Wallonie-Bruxelles funded by the Walloon Region (Grant No. 1117545).
A.C.G.C. acknowledge the support from the GridUIS-2 experimental testbed, developed under the Universidad Industrial de Santander (SC3-UIS) High Performance and Scientific Computing Centre, with support from UIS Vicerrectoría de Investigación y Extensión (VIE-UIS) and several UIS research groups as well as other funding resources.

APPENDIX A: CHARGE DISTRIBUTION WITHIN A CASHEW

Figure 2d revealed an asymmetric shape of the charge density within a cashew. However, this and most topographic images taken in this study do not allow to directly resolve the Te-trimerization within a cashew. Figure A1a shows a topographic image of the {010} surface of a $NbTe_4$ sample for which a clear separation of the charge density within the cashews is resolved. The FFT of this figure (fig. A1b) reproduces the main features of the CDW superstructure, particularly the $(0, 2c^*/3)$ peak splitting (in red circles). Fig A1c shows an expanded view of one of the cashews in fig. A1a, revealing its internal structure. Three different maxima in the charge density can be observed (green circles), consistent with the presence of three Te-atoms in each cashew. Two of those maxima are on the right side of the cashew and are

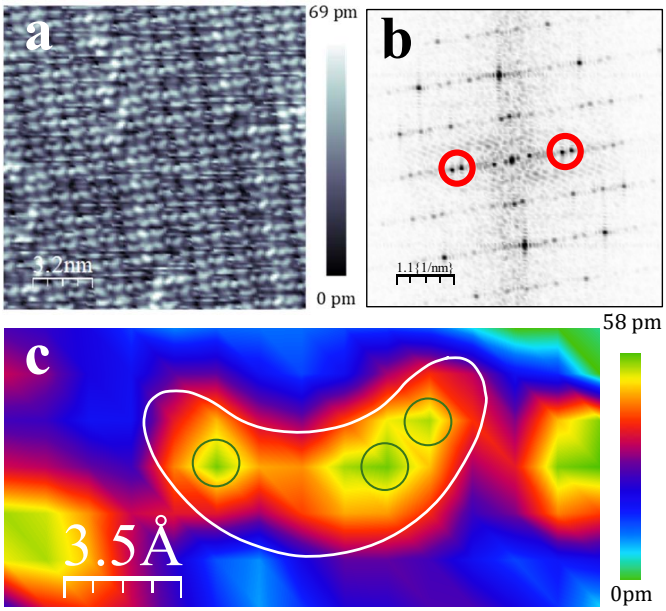

FIG. A1. (Color online) **(a)** Topographic image of $NbTe_4$ in which the internal structure of the charge distribution within the cashews can be resolved. **(b)** FFT of the image in (a). The $(0, 2c^*/3)$ split-peaks are highlighted in red circles. **(c)** Expanded view of one of the cashews in (a), in which three maxima of the charge density can be clearly resolved (green circles). This is consistent with the presence of three Te-atoms per cashew.

close to each other, and the other maximum is on the left side, further apart from the other two. This leads to the asymmetric average charge distribution within a cashew observed for the other topographic images with less resolution, and to the conclusion that the trimerization of the Te-atoms in the surface is originated in the trimerization of the Nb-atoms just underneath the surface, as discussed in section 3.3.

APPENDIX B: DOMAIN WALLS AND FFT PEAK SPLITTING

The peak splitting observed in the FFT of the topographic images, particularly of the $(0, 2c^*/3)$ peaks, are not a consequence of a periodic arrangement of domain walls, but instead, of the phase-slip along a large number of chains, as illustrated in Fig. A2. In order to prove this, we select two small regions of the 15 nm × 15 nm topographic image in fig. A2(a). The first region, enclosed by a green square (fig. A2b), shows no domain walls. Its corresponding FFT (fig. A2c) does not show evidence of splitting of the $(0, 2c^*/3)$ peaks (circled in red). The second region, enclosed by a red square (fig. A2d), contains only one domain-wall that extends along all the 15 chains that form the image. Its corresponding FFT (fig. A2e) shows a clear splitting of the $(0, 2c^*/3)$

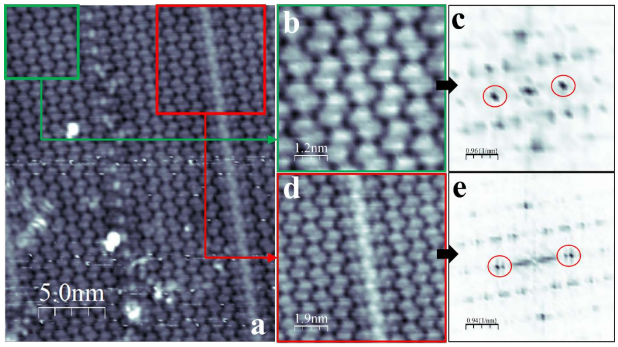

FIG. A2. (Color online) **(a)** Large topographic image of $NbTe_4$ in which two smaller areas are selected and expanded. **(b)** Highlights the region enclosed by the green square in (a), in which no domain walls can be identified. **(c)** shows the FFT of the image in (b). No peak splitting is recognized for the $(0, 2c^*/3)$ peaks circled in red. **(d)** Highlights the region enclosed by the red square in (a), in which a single domain wall can be identified. **(e)** shows the FFT of the image in (d), with a clear splitting in the $(0, 2c^*/3)$ peaks circled in red.

peaks, plus additional features in other locations of the reciprocal space.

Different types of domain walls can be recognized in this material. As mentioned in the discussion section, intrachain CDW phase-slips of $\pm 2n\pi/3$ are the only ones allowed, but different combinations of phase-slips in adjacent chains can create different possibilities for domain wall configurations. Figure A3 shows five different examples of domain walls and their respective FFTs, in addition to the two discussed in fig. 5. For all of these domain walls, a splitting in the $(0, 2c^*/3)$ peaks is clearly observed.

APPENDIX C: SPECTROSCOPY CURVE IN THE CDW STATE

Figure A4 shows a representative tunneling conductance vs bias voltage curve taken at a temperature of 1.7 K. In this region a gap-like feature, with $2\Delta \approx 24$ meV is observed, similar to the gap-like feature recently measured in $TaTe_4$ at 4.2 K in ref. [6]. In that work, the gap of $2\Delta \approx 23$ meV is ascribed to a new surface CDW modulation with a q-vector distinct from the one of the bulk CDW modulation, $(0, 2c^*/3)$. We do not observe such a surface modulation in $NbTe_4$. However, we do observe the same gap spectral feature as in $TaTe_4$. This fact suggests the existence of other low-energy electronic excitations that are common to both, $NbTe_4$ and $TaTe_4$, not necessarily associated with a CDW instability.

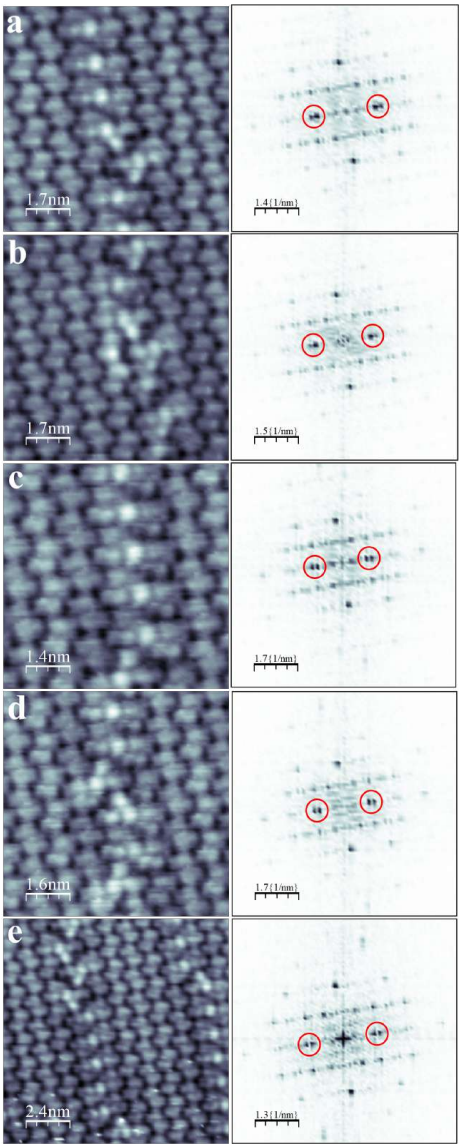

FIG. A3. (Color online) Topographic images (left-column figures) around different domain walls found in our $NbTe_4$ samples, and their corresponding FFTs (right-column figures). Al FFTs show the splitting of the $(0, 2c^*/3)$ peaks, circled in red.

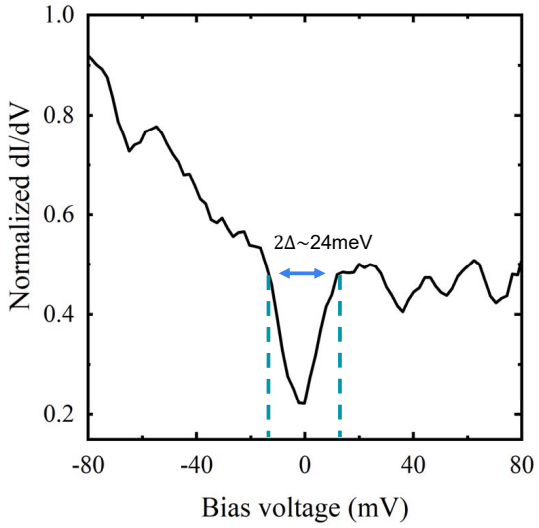

FIG. A4. (Color online) Tunneling conductance vs bias voltage curve taken at T = 1.7 K. A gap-like spectral feature of $2\Delta \approx 24$ meV can be observed, similar to recent results in $TaTe_4$ [6].

[1] S. Manzeli, D. Ovchinnikov, D. Pasquier, O. V. Yazyev, and A. Kis, 2D transition metal dichalcogenides, Nature Reviews Materials **2**, 17033 (2017).

[2] P. Monceau, Electronic crystals: an experimental overview, Advances in Physics **61**, 325 (2012).

[3] B. de Lima, N. Chaia, T. Grant, L. de Faria, J. Canova, F. de Oliveira, F. Abud, and A. Machado, Large enhancement of the CDW resistivity anomaly and traces of superconductivity in imperfect samples of $NbTe_4$, Materials Chemistry and Physics **226**, 95 (2019).

[4] X. Zhang, Q. Gu, H. Sun, T. Luo, Y. Liu, Y. Chen, Z. Shao, Z. Zhang, S. Li, Y. Sun, Y. Li, X. Li, S. Xue, J. Ge, Y. Xing, R. Comin, Z. Zhu, P. Gao, B. Yan, J. Feng, M. Pan, and J. Wang, Eightfold fermionic excitation in a charge density wave compound, Phys. Rev. B **102**, 035125 (2020).

[5] J. Gooth, B. Bradlyn, S. Honnali, and et al., Axionic charge-density wave in the weyl semimetal $(TaSe_4)I_2$, Nature **575**, 315âĂŞ319 (2019).

[6] H. Sun, Z. Shao, T. Luo, Q. Gu, Z. Zhang, S. Li, L. Liu, H. Gedeon, X. Zhang, Q. Bian, J. Feng, J. Wang, and M. Pan, Discovery of an unconventional charge modulation on the surface of charge-density-wave material $TaTe_4$, New Journal of Physics **22**, 083025 (2020).

[7] F. W. Boswell, A. Prodan, and J. K. Brandon, Charge-density waves in the quasi-one-dimensional compounds NbTe4 and $TaTe_4$, Journal of Physics C: Solid State Physics **16**, 1067 (1983).

[8] M. B. Walker, A model for charge-density waves in $TaTe_4$ and related materials, Canadian Journal of Physics **63**, 46 (1985).

[9] X. Yang, Y. Zhou, M. Wang, H. Bai, X. Chen, C. An, Y. Zhou, Q. Chen, Y. Li, Z. Wang, J. Chen, C. Cao, Y. Li, Y. Zhou, Z. Yang, and Z.-A. Xu, Pressure induced superconductivity bordering a charge-density-wave state in $NbTe_4$ with strong spin-orbit coupling, Scientific Reports **8**, 6298 (2018).

[10] Y. Yuan, W. Wang, Y. Zhou, X. Chen, C. Gu, C. An, Y. Zhou, B. Zhang, C. Chen, R. Zhang, and Z. Yang, Pressure-induced superconductivity in topological semimetal candidate $TaTe_4$, Advanced Electronic Materials **6**, 1901260.

[11] T. Ikari, H. Berger, and F. Levy, Electrical properties of $NbTe_4$ and $TaTe_4$, physica status solidi (b) **139**, 10.1002/pssb.2221390143 (1987).

[12] S. Tadaki, N. Hino, T. Sambongi, K. Nomura, and F. LÃľvy, Electrical properties of $NbTe_4$ and $TaTe_4$, Synthetic Metals **38**, 227 (1990).

[13] K. Selte and A. Kjekshus, On the Crystal Structure of $NbTe_4$, Acta Chemica Scandinavica **18**, 690 (1964).

[14] M. B. Walker and R. Morelli, $NbTe_4$: A model for a class of incommensurate-to-incommensurate phase transitions, Phys. Rev. B **38**, 4836 (1988).

[15] A. Prodan and F. W. Boswell, A dualistic interpretation of the incommensurate modulated structures of $NbTe_4$, Acta Crystallographica Section B **43**, 165 (1987).

[16] D. J. Eaglesham, D. Bird, R. L. Withers, and J. W. Steeds, Microstructural behaviour in the CDW states of $NbTe_4$ and $TaTe_4$ domains, discommensurations and superlattice symmetry, Journal of Physics C: Solid State Physics **18**, 1 (1985).

[17] F. W. Boswell and A. Prodan, Structural changes in the discommensurate distortion waves of $NbTe_4$ on cooling, Phys. Rev. B **34**, 2979 (1986).

[18] A. Prodan, S. W. Hla, V. Marinković, H. Böhm, F. W. Boswell, and J. C. Bennett, Scanning tunneling microscope study of charge-density-wave modulations in $NbTe_4$, Phys. Rev. B **57**, 6235 (1998).

[19] P. Hohenberg and W. Kohn, Inhomogeneous electron gas, Phys. Rev. **136**, B864 (1964).

[20] W. Kohn and L. J. Sham, Self-consistent equations including exchange and correlation effects, Phys. Rev. **140**, A1133 (1965).

[21] X. Gonze, B. Amadon, P.-M. Anglade, J.-M. Beuken, F. Bottin, P. Boulanger, F. Bruneval, D. Caliste, R. Caracas, M. CÃťtÃľ, T. Deutsch, L. Genovese, P. Ghosez, M. Giantomassi, S. Goedecker, D. Hamann, P. Hermet, F. Jollet, G. Jomard, S. Leroux, M. Mancini, S. Mazevet, M. Oliveira, G. Onida, Y. Pouillon, T. Rangel, G.-M. Rignanese, D. Sangalli, R. Shaltaf, M. Torrent, M. Verstraete, G. Zerah, and J. Zwanziger, Abinit: First-principles approach to material and nanosystem properties, Computer Physics Communications **180**, 2582 (2009).

[22] X. Gonze and et al., The abinitproject: Impact, environment and recent developments, Computer Physics Communications **248**, 107042 (2020).

[23] M. J. van Setten, M. Giantomassi, E. Bousquet, M. J. Verstraete, D. R. Hamann, X. Gonze, and G.-M. Rignanese, The PseudoDojo: Training and grading a 85 element optimized norm-conserving pseudopotential table, Comput. Phys. Commun. **226**, 39 (2018).

[24] J. P. Perdew, A. Ruzsinszky, G. I. Csonka, O. A. Vydrov, G. E. Scuseria, L. A. Constantin, X. Zhou, and K. Burke, Restoring the density-gradient expansion for exchange in solids and surfaces, Phys. Rev. Lett. **100**, 136406 (2008).

[25] X. Gonze and C. Lee, Dynamical matrices, born effective charges, dielectric permittivity tensors, and interatomic force constants from density-functional perturbation theory, Phys. Rev. B **55**, 10355 (1997).

[26] D. Orobengoa, C. Capillas, M. I. Aroyo, and J. M. Perez-Mato, *AMPLIMODES*: symmetry-mode analysis on the Bilbao Crystallographic Server, Journal of Applied Crystallography **42**, 820 (2009).

[27] I. Fisher, M. Shapiro, and J. Analytis, Principles of crystal growth of intermetallic and oxide compounds from molten solutions, Philosophical Magazine **92**, 2401 (2012).

[28] B. Guster, M. Pruneda, P. OrdejÃşn, and E. Canadell, Competition between Ta-Ta and Te-Te bonding leading to the commensurate charge density wave in $TaTe_4$ (2021), arXiv:2111.10828 [cond-mat.mtrl-sci].

[29] A. Prodan, F. W. Boswell, J. C. Bennett, J. M. Corbett, T. Vidmar, V. Marinković, and A. Budkowski, Structures of two low-temperature incommensurate $NbTe_4$ phases, Acta Crystallographica Section B **46**, 587 (1990).

[30] J. Mahy, J. Van Landuyt, S. Amelinckx, Y. Uchida, K. D. Bronsema, and S. Van Smaalen, Direct observation of discommensuration arrays in $nbte_4$ by means of low-temperature electron microscopy, Phys. Rev. Lett. **55**, 1188 (1985).

[31] D. W. Bullett, p-d band overlap and the electronic structure of $NbTe_4$, Journal of Physics C: Solid State Physics **17**, 253 (1984).

[32] L. Vicarelli, S. J. Heerema, C. Dekker, and H. W. Zandbergen, Controlling defects in graphene for optimizing the electrical properties of graphene nanodevices, ACS Nano **9**, 3428 (2015).

[33] A. Fang, J. A. W. Straquadine, I. R. Fisher, S. A. Kivelson, and A. Kapitulnik, Disorder-induced suppression of charge density wave order: Stm study of pd-intercalated $ErTe_3$, Phys. Rev. B **100**, 235446 (2019).

[34] P.-J. Hsu, T. Mauerer, M. Vogt, J. J. Yang, Y. S. Oh, S.-W. Cheong, M. Bode, and W. Wu, Hysteretic melting transition of a soliton lattice in a commensurate charge modulation, Phys. Rev. Lett. **111**, 266401 (2013).

[35] G. Grüner, The dynamics of charge-density waves, Rev. Mod. Phys. **60**, 1129 (1988).

[36] M. D. Johannes and I. I. Mazin, Fermi surface nesting and the origin of charge density waves in metals, Phys. Rev. B **77**, 165135 (2008).

[37] V. Parente, A. Tagliacozzo, F. von Oppen, and F. Guinea, Electron-phonon interaction on the surface of a three-dimensional topological insulator, Phys. Rev. B **88**, 075432 (2013).

[38] R. Heid, I. Y. Sklyadneva, and E. V. Chulkov, Electron-phonon coupling in topological surface states: The role of polar optical modes, Scientific Reports **7**, 1095 (2017).

[39] C. A. C. Garcia, D. M. Nenno, G. Varnavides, and P. Narang, Anisotropic phonon-mediated electronic transport in chiral weyl semimetals, Phys. Rev. Materials **5**, L091202 (2021).